Friction

Research Article

Influence of slip ratio on the phase stability of austenitic steel AISI 304 during rolling contact wear

Miroslav Neslušan[1,✉], Ronald Bašťovanský[1], Peter Minárik[2,4], Karel Trojan[3], Zuzana Florková[4], Katarína Zgútová[5]

Cite this article: Neslušan M, Bašťovanský R, Minárik P, et al. *Friction* 2026, **14**(5): 9441203. https://doi.org/10.26599/FRICT.2025.9441203

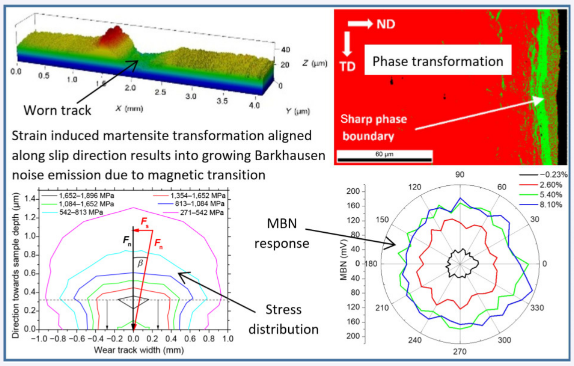

ABSTRACT: This study uses rollers with curved profiles to explore the phase stability of austenitic matrix AISI 304 exposed to the rolling contact wear under the variable slip ratios in the range from −0.23% up to 8.81%. The wear track is formed under the cyclic surface delamination and the asymmetric extrusion of matrix towards the track side. The size of wear track and the fraction of extruded materials grow along with the slip ratio. Severe plastic deformation makes the parental matrix susceptible to phase transition when the ferromagnetic martensite replaces the paramagnetic austenite. The extent of this transition and the preferential alignment of neighbouring phases were found to be more complex under the higher slip ratios. The matrix is preferentially strained along the wear track width when the slip ratio is close to zero, whereas the presence of friction components at the higher slip ratios preferentially strains the matrix closer to the rolling direction (RD). The sandwich-like microstructure is formed when the extremely refined layer containing a mixture of strain-induced martensite (SIM) and austenite on the free surface is replaced by the thermally softened one due to friction heating, containing mostly strain-induced martensite, followed by the plastically strained region with prevailing austenite fraction. The heat release due to plastic deformation of austenite, phase transformation, and friction contributes to elevated temperatures, especially at the higher slip ratios. The enhanced thermal softening at the higher slip ratios reduces the compressive residual stresses, but the dislocation density in austenite as well as martensite is increasing. The study also demonstrates that this phase transformation can be reliably monitored by magnetic Barkhausen noise (MBN), which increases with the slip ratio due to the growing preferential straining of both phases into the direction of rolling. The high sensitivity of this non-destructive magnetic method is based on the medium-increasing fraction of the strain-induced martensite and its distinct preferential straining along the rolling direction at higher strain rates. The influence of residual stress state on magnetic emission is only minor.

KEYWORDS: austenitic matrix; phase transition; slip ratio; rolling; strain-induced martensite (SIM); Barkhausen noise (MBN)

1 Introduction

Austenitic steels are widely utilized in industrial and engineering applications due to their exceptional malleability, corrosion resistance, and ability to withstand aggressive environments, combined with prolonged work hardening. The stability of the fcc lattice at room temperature is governed by the chromium and nickel additions [1, 2], as summarised in the Schaeffler-Delong diagram. Components made of austenitic steel often undergo cold working processes of various types to refine grain structure of the matrix or/and increase their yield and ultimate strength at the expense of reduced malleability [3, 4]. However, plastic deformation of austenitic steels can also activate the strain-induced martensite (SIM) transformation when the bcc regions' size, density, and the corresponding volume fraction depend on the cold work nature, like conditions, duration, etc. [5–7]. Furthermore, the extent of this phase transformation is also strongly affected by the martensitic transformation temperature (usually lying above room temperature) and matrix chemistry, particularly the concentration of austenite-stabilizing elements that enhance the stability of the parent lattice.

Martensite phase transformation primarily occurs in the

[1] Faculty of Mechanical Engineering, University of Žilina, Univerzitná 1, 01026 Žilina, Slovakia. [2] Charles University, Faculty of Mathematics and Physics, Ke Karlovu 5, 12116 Praha 2, Czech Republic. [3] Faculty of Nuclear Sciences and Physical Engineering, Czech Technical University in Prague, Trojanova 13, 12000 Praha, Czech Republic. [4] Research Center, University of Žilina, Univerzitná 1, 01026 Žilina, Slovakia. [5] Faculty of Civil Engineering, University of Žilina, Univerzitná 1, 01026 Žilina, Slovakia.

✉ Corresponding author. E-mail: miroslav.neslusan@fstroj.uniza.sk

Received: March 23, 2025; Revised: July 25, 2025; Accepted: December 12, 2025

austenite shear band intersections, and the nuclei grow with an increasing plastic strain [8, 9]. It is widely accepted that the martensite nuclei can be found at the lattice imperfections generating local stress concentration zones. The SIM is usually an athermal process when the Shockley partial dislocations accumulate. Once the accumulation of these dislocations attains the critical value, the martensite nuclei form during plastic deformation [10].

The SIM transformation in austenitic steels has been observed under a variety of deformation processes, being volumetric in nature or limited to the near-surface region when the steep microstructure gradient towards the bulk can be observed. Uniaxial or biaxial tension [11–13], shot peening [14, 15], friction wear [7], rolling contact wear [16], angular pressing [17], high-pressure torsion [18, 19], or forging [20, 21] cases reported that the alterations of austenitic matrix can be quite complex, including austenitic grains fragmentation, phase transformations, stress redistribution, etc.

The austenitic matrix is fully paramagnetic in contrast to the ferromagnetic nature of the strain-induced martensite. Therefore, applying magnetic methods for the abovementioned phenomenon is challenging because of the prominent change in the magnetic behavior. Random magnetic orientation in the austenite is distinctly different from the long-distance magnetic order in magnetic domains of the martensite matrix, separated by domain walls (DWs). Alterations in the external magnetic field and/or mechanical stress within the matrix initiate irreversible DWs motion [22, 23]. These DWs produce acoustic and electromagnetic pulses during their discontinuous motion, which are detectable on a material surface and are known as Barkhausen noise (MBN) [22, 23]. DWs are pinned in their positions due to the presence of lattice imperfections such as dislocation tangles [24, 25], grain boundaries [26, 27], precipitates [28, 29], and hard magnetic phase [30]. The Barkhausen noise signal, therefore, contains information about these microstructure features, and the Barkhausen noise technique can be employed for monitoring ferromagnetic components in a variety of applications.

In addition to its application in monitoring grinding damage, the use of Barkhausen noise emission in the study of strain-induced martensitic transformation in austenitic steel represents one of the most sensitive implementations of this technique. While the high sensitivity of MBN in detecting grinding burn is primarily attributed to matrix softening (a reduction in dislocation density) accompanied by an increase in the amplitude of tensile stresses [31–33], its application in austenitic steels is directly correlated with the extent of phase transformation and the associated magnetic changes [7, 12, 16, 34]. MBN has already been employed to monitor SIM transformation in austenitic steels after cold working, such as shot peening [14, 34], friction wear [7], uniaxial or biaxial tension [12, 13], or rolling contact wear [16]. These studies proved the excellent potential of MBN for such a topic.

Our previous study investigated the influence of rolling contact wear in AISI 304 as a function of rolling process duration [16]. It was reported that the increase in the MBN signal with prolonged rolling time correlates with a higher volume fraction of SIM. A good correlation between the extent of phase transformation and the MBN signal, in contrast with the X-ray diffraction (XRD) technique, is due to the larger interaction volume of the MBN technique. This study was focused on the pure rolling process without a significant slip between the sample and the two rollers. However, it is well known that rolling wear can be substantially accelerated when the superimposing slip in the moving contact is integrated [35–41].

Tosangthum et al. [35] reported that the matrix becomes more strained under the rolling/sliding regime, the wear rate is accelerated, and microcracks on the surface follow the shear component in the rolling/sliding interface. Yang et al. [36] investigated the influence of slip control on wheel wear. Argatov and Chai [37] reported on a theoretical justification of the slip index concept in fretting analysis. Wang et al. [38] provided a numerical model to simulate the transient frictional viscoelastic sliding contact. Lian et al. [39] found that the rolling contact fatigue life is significantly reduced under the higher slip ratios due to the increasing temperature and the decreasing strength of the matrix. Gao et al. [40] investigated the evolution of tribo-magnetization during the sliding of ferromagnetic materials. Zhao and Wong [41] investigated shear heating under high slide-to-roll ratios.

The previous study has already discussed the phase transformation of AISI 304 under the pure rolling contact wear as a function of rolling duration. Consequently, the high potential of the MBN technique for monitoring this experiment has been clearly proved. However, the related studies in this field demonstrated that rolling contact wear can be severely accelerated when superimposing sliding is considered. To examine the influence of a variable slip ratio, this study explores the effects of gradually increasing the sample's rotational speed, rather than solely relying on the roller speed, to introduce a shear component at the sample/roller interface.

2 Experimental

The samples for experimental works were manufactured from the austenitic stainless steel AISI 304. Its mechanical properties are listed in Table 1, and its chemical composition in Table 2.

The employment of AISI 304 for experimental work is due to its high susceptibility to SIM formation related to the chemical composition and the corresponding stacking fault energy (SFE). With the chemical composition as listed in Table 2, SFE can be easily calculated 14.04 $mJ \cdot m^{-2}$ [42, 43]. Such low SFE (below 20 $mJ \cdot m^{-2}$) favors predominance of SIM during work hardening of the employed AISI 304 instead of twining and/or dislocations gliding. For example, SFE is about 50 $mJ \cdot m^{-2}$ for AISI 316, and SIM in this steel is significantly attenuated [42]. Earlier published studies [16, 34, 44] also indicated that the direct $\gamma \rightarrow \alpha'$ phase transformation should be expected without the non-ferromagnetic ε phase. Furthermore, it is considered that during rolling with an

Table 1 Mechanical properties of AISI 304

Yield strength (MPa)	Ultimate strength (MPa)	Modulus of elasticity (GPa)	HV	Poisson's ratio
190	600	195	129	0.29

Table 2 Chemical composition of AISI 304 (unit: wt%)

Chemical composition	Fe	C	Mn	Si	Cr	S	Ni	P	N	Mo
Content	Bal.	0.07%	2%	1%	18.5%	0.03%	9.25%	0.05%	0.10%	0.32%

integrated slip ratio, SIM formation is substantially accelerated due to multiaxial loading. Also, much higher Md30/50 about −82 °C for the employed AISI 304 indicates lower stability of austenite against formation of SIM as contrasted against AISI 316 having Md30/50 about −176 °C [42].

AISI 304 was delivered in the form of a bar with a diameter of 70 mm. The bar was sectioned by the band saw into specimens of width 15 mm. The final shape and geometry of the investigated samples (Fig. 1(a)) were manufactured by turning using the TNMG insert at a cutting speed of 140 m·min^{-1}, cutting depth 0.25 mm, and feed 0.09 mm (the final width of 13 mm, inner diameter of 36 mm, and outer diameter of 66 mm) followed by the milling cycle to produce the groove for transmission of the torque from the asynchronous motor 4AP632s. Afterward, the samples were fixed on the shaft between the roller and supporting wheel (Figs. 1(b) and 2), both of diameter 146 mm. Their position was fixed with respect to the axial direction by the aluminium disk and the screw (Fig. 2). The shaft was equipped with the screw (Fig. 1(b)) in order to avoid slipping between the shaft and the sample via the milled groove. The roller was made of the quenched high-speed steel (hardness 63±1.5 HRC) of the geometry illustrated in Fig. 3. The supporting wheel was made of aluminum alloy. Due to the significant differences in the mechanical properties of the counteracting components as well as with respect to their specific shape (especially the curvature profile of the roller and the flat profile of the supporting wheel), the produced wear track on the samples during the experiment is a result of the severe plastic deformation in the roller/sample interface only (the roller shape, as well as its dimensions, are unaffected during the test).

Experiments were carried out on the rolling machine illustrated in the previous study [16]. The normal component, F_n, in the roller/sample interface was generated by the gravitational load of 1,002 N. The shear component F_f in this interface was obtained as a result of the different speeds of the roller and sample in the rolling direction (RD), which resulted in the variable slip ratios (Fig. 4). The speed of the roller was kept constant at 130.5 m·min^{-1}. In contrast, the rotational speed of the sample was altered (Table 3). The speed of the roller and the samples were measured throughout the loading time using a digital tachometer (DT2235A, Shenzhen Graigar Technology Co., Ltd., China).

Transmission of the torque from the asynchronous motor to the sample was made via the toothed belt, and the asynchronous motor was controlled by a frequency converter (ATV11HU05M2E, Telematique, France). The test duration for each slip ratio was 52.5 s (for each slip ratio, three samples were rolled) to investigate the surface state in the region of the strengthening stage (the region in which torque M_k attains the maximum) (Fig. 5).

The aforementioned rolling conditions were suggested in order to demonstrate the influence of the slip ratio and, therefore, the synergistic contribution of the shearing in the roller/sample interface on the AISI 304 rolling/sliding wear.

For this reason, during the preliminary phase of this study, the influence of many variables, such as rotational speeds, mass load, time duration, and curvature of the roller, was tested. The depth and extent of AISI 304 surface damage were linked with the phase transformation austenite → martensite and detected by Barkhausen noise emission.

An Empyrean diffractometer (Series 3, Malvern Panalytical B.V., the Netherlands) was used for XRD. Co, Mn, and Mo radiations with point focus (meant Co Kα, etc.) were used to obtain the XRD patterns. The crystallite size and microstrain were

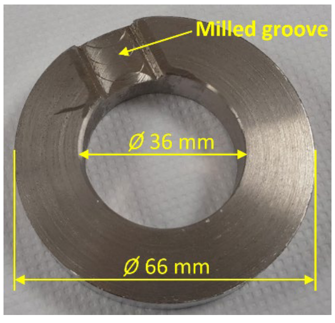

(a) Sample

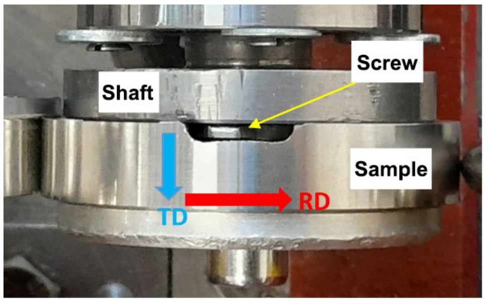

(b) Sample clamping

Fig. 1 Sample with the milled groove and its clamping on the shaft.

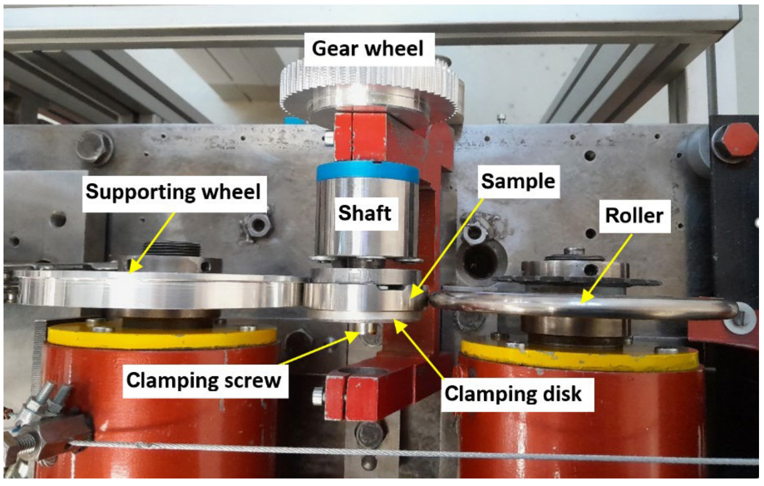

Fig. 2 The sample mounted on the shaft between the curved roller and the supporting disk.

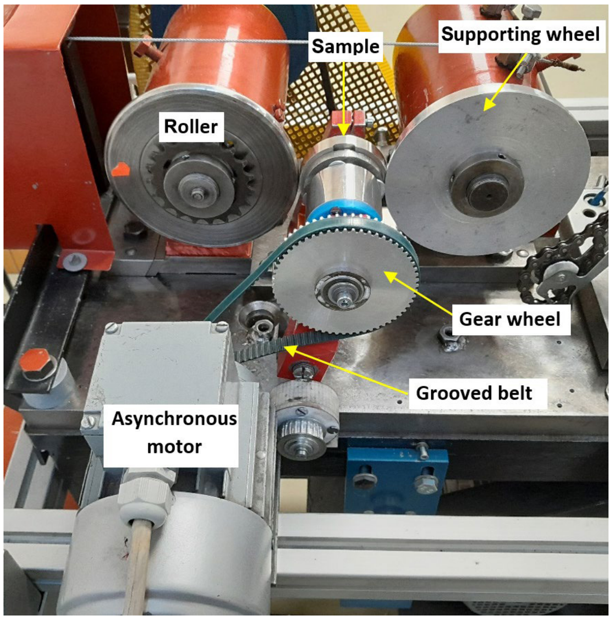

Fig. 3 Transmission of the torque from the asynchronous motor to the sample via the gear wheels and the grooved belt.

determined from diffraction patterns using the Rietveld refinement performed in MStruct software. The density of dislocation was calculated according to Williamson's and Smallman's method. The errors result from the Rietveld refinement calculation method. For the determination of macroscopic residual stresses (RS), Mn and Cr radiation with point focus were used to investigate the austenite and ferrite phases. The RS values were calculated from the lattice deformations, which were determined based on the experimental dependencies of $2\theta(\sin^2\psi)$ assuming a biaxial RS condition, where θ is the Bragg angle, and ψ is the angle between the diffracting lattice planes and the sample surface. The positions of the diffraction doublet $K\alpha_1\alpha_2$ planes {311} and {211} of the austenite and ferrite phases were obtained by fitting the maxima with two Pearson VII functions. The X-ray elastic constants $s_1 = -1.87$ TPa^{-1} and $½s_2 = 6.98$ TPa^{-1} for the austenite phase and $s_1 = -1.25$ TPa^{-1} and $½s_2 = 5.76$ TPa^{-1} for the ferrite phase were used to calculate RS using the Winholtz and Cohen method. For further XRD test parameters (Table 4). The errors shown below are attributed to the least-square method, i.e., non-linearity of $2\theta(\sin^2\psi)$ function. The irradiated volume was determined by the Bragg-Brentano geometry of the diffractometer, the effective penetration depth of

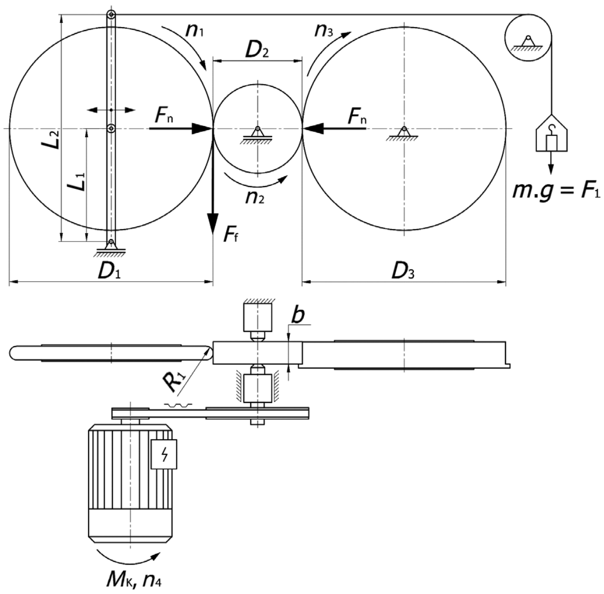

$D_1 = D_3$ (mm)	D_2 (mm)	R_1 (mm)	b (mm)	L_1 (mm)	L_2 (mm)	m (kg)	F_1 (N)	F_n (N)	$i = n_4/n_2$ (—)
146	66	4.93	16	145	75	52.83	518	1,002	4

Fig. 4 Brief sketch of the rolling system.

Table 3 Rotational speeds of the roller and the samples, and the corresponding slip ratio

Roller revolutions (min^{-1})	285	285	285	285
Sample revolutions (min^{-1})	628	646	665	685
Engine revolutions (min^{-1})	—	2,585	313	2,739
Supporting wheel revolutions (min^{-1})	295	304	301	322
Supporting wheel speed (min^{-1})	129.9	133.7	137.7	141.7
Roller speed (m·min^{-1})	130.5	130.5	130.5	130.5
Sample speed (m·min^{-1})	130.2*	134.0	138.0	142.0
Slip ratio (%)	−0.23*	2.60	5.40	8.10

Note: * The sample speed of 130.5 m·min^{-1} set up before the pure rolling load was slowed down to 130.2 m·min^{-1} during the real rolling due to the small slip in the roller/sample interface when the rolling from the roller was transmitted to the sample (this results in the negative slip ratio −0.23%).

Table 4 Further XRD test parameters

Test	Anode type	Wavelength	Range	Scan speed	$\sin^2\psi$
Pole figure	Co	0.1790307 nm	0°–35°, χ	1	—
			45°–105°, 2θ	0.00022 (°)/s	—
XRD pattern	Mo	0.0710749 nm	17°–75°, 2θ	0.00033 (°)/s	—
	Mn	0.2103190 nm	58°–132°, 2θ	0.00027 (°)/s	—
Residual stress			145°–160°, 2θ	0.08 (°)/s	±0, 0.1, …, 0.5
	Cr	0.2291062 nm	149°–162°, 2θ	0.024 (°)/s	

the X-ray radiation, and the slit used, which was 0.25 mm high and 1 mm wide for the transverse direction (TD) and 0.3 mm high and 0.3 mm wide for the RD.

Microhardness measurements HV0.025 were carried out using the device (Qness Q10, QATM, Austria) (4 repetitive measurements).

The microstructure analysis of the affected surface was performed by a scanning electron microscope (SEM; Auriga Compact, ZEISS, Japan) equipped with an electron backscatter diffraction (EBSD; EDAX, USA) camera. The samples for EBSD were cut along cross-section and longitudinal sections of the deformed zone and subsequently mechanically polished with decreasing particle size down to 50 nm. The measured data sets were partially reindexed by Spherical indexing in the OIM TSL 9 software.

The produced track topography was observed by the use of a laser scanning confocal microscope (LSM 700, Zeiss, Germany) with the laser wavelength 405 nm under magnification 500×, applying the z-Stack function in software Zen black (scanning window size 4.1 mm × 0.6 mm). The primary profiles obtained during the surface scanning were post-processed (filtered with respect to the ISO standard) in order to extract surface roughness profiles and the corresponding surface roughness parameters (the cut-off wavelengths 0.8 mm). Surface roughness parameters were analyzed in RD and TD directions; the provided average and standard deviation values were calculated from the 10 repetitive measurements.

The shear force F_f in the sample/roller interface was calculated based on the measured asynchronous motor current. Information about the current (obtained from the clamp mustimeter FLUKE 325) was recorded and stored in the digital oscilloscope (TDS 2004C, Tektronix, USA), converted into the torque when the calibration relationships between the current and torque were established in the dynamic brake Dynofit M440.

Barkhausen noise measurements were carried out in the RD as well as TD (Fig. 1(b)). The normal direction (ND) is perpendicular to RD as well as TD and represents the direction from the surface towards the deeper subsurface and bulk regions. Thirty-five measurements in both directions were taken on each sample with a regular step of 10°, and the polar graphs of the extracted MBN features were plotted. Magnetizing and other conditions with respect to MBN measurements are listed in Table 5.

Table 5 The conditions of MBN measurements

Magnetizing frequency (Hz)	125
Magnetizing field (kA·m^{-1})	±9.8
Low pass filter (Hz)	50
High pass filter (Hz)	1,000
Sensor	S1-18-12-01
Device	RollScan 350
Software	MicroScan 5.4.1
Sampling frequency (MHz)	6.4

The filtered Barkhausen noise emission was used to count detected pulses, calculate the effective value of the signal (reported as MBN), analyze Barkhausen noise envelopes, and extract features such as PP and PH. PP refers to the magnetic hardness of a body and represents the magnetic field in which an envelope attains the maximum. PH is the maximum of MBN envelope. The true information about MBN originating from the investigated surface, only U_{tru} was calculated from the measured Barkhausen noise emission U_{mea}, following Eq. (1) in order to subtract the contribution of mechanical vibration during the cyclic magnetization U_{vib} and Barkhausen noise originating from the sensor U_{sen} [45].

$$U_{\text{tru}} = \sqrt{U_{\text{mea}}^2 - U_{\text{vib}}^2 - U_{\text{sen}}^2} \tag{1}$$

U_{sen} is constant and equal to 29.56 mV, whereas U_{vib} was subtracted from U_{mea} by applying the low-pass filter of 50 Hz (this value was set by analyzing the fast Fourier transform (FFT) spectra of the raw MBN signals).

3 Results of experiments and their discussion

3.1 Torque, wear track profile, and surface roughness

The shear force F_f in the sample/roller interface can be calculated based on the measured torque of the asynchronous motor $M_{k\text{-motor}}$ and the well-known gear ratio $i = n_4/n_2$, where n_4 is the engine revolutions and n_2 is the sample revolutions (Fig. 4 and Table 3). Torque on the sample M_k can be obtained as Eqs. (2) and (3):

$$M_{\text{k}} = M_{\text{k-motor}} \times i = M_{\text{k}} \times \frac{n_4}{n_2} \tag{2}$$

Then, F_f is based on Eq. (3):

$$M_{\text{k}} = 0.5 \times F_{\text{f}} \times D_2 \rightarrow F_{\text{f}} = \frac{2 \times M_{\text{k}}}{D_2} \tag{3}$$

The friction coefficient $\mu = F_n/F_f$ and the heat developed in the sample/roller interface with respect to the presence of F_f component Q_f can be calculated as Eq. (4):

$$Q_{\text{f}} = F_{\text{f}} \times v_{\text{c2}} \tag{4}$$

where v_{c2} is the sample speed.

As depicted in Fig. 5, the measured M_k clearly demonstrates that the ascending phase of M_k is followed by the descending one, and the cyclic behaviour was measured for all slip ratios. The progressive ascent of M_k in time is caused by the surface strengthening originating from the work hardening of the austenite, as well as the superimposing contribution of phase transformation related to the formation of the SIM. The mechanical energy of the rolling is consumed and accumulated within the narrow contact region. As soon as the consumed energy attains the critical threshold, the plasticity of the sample matrix in the sample/roller interface is fully exhausted, and M_k

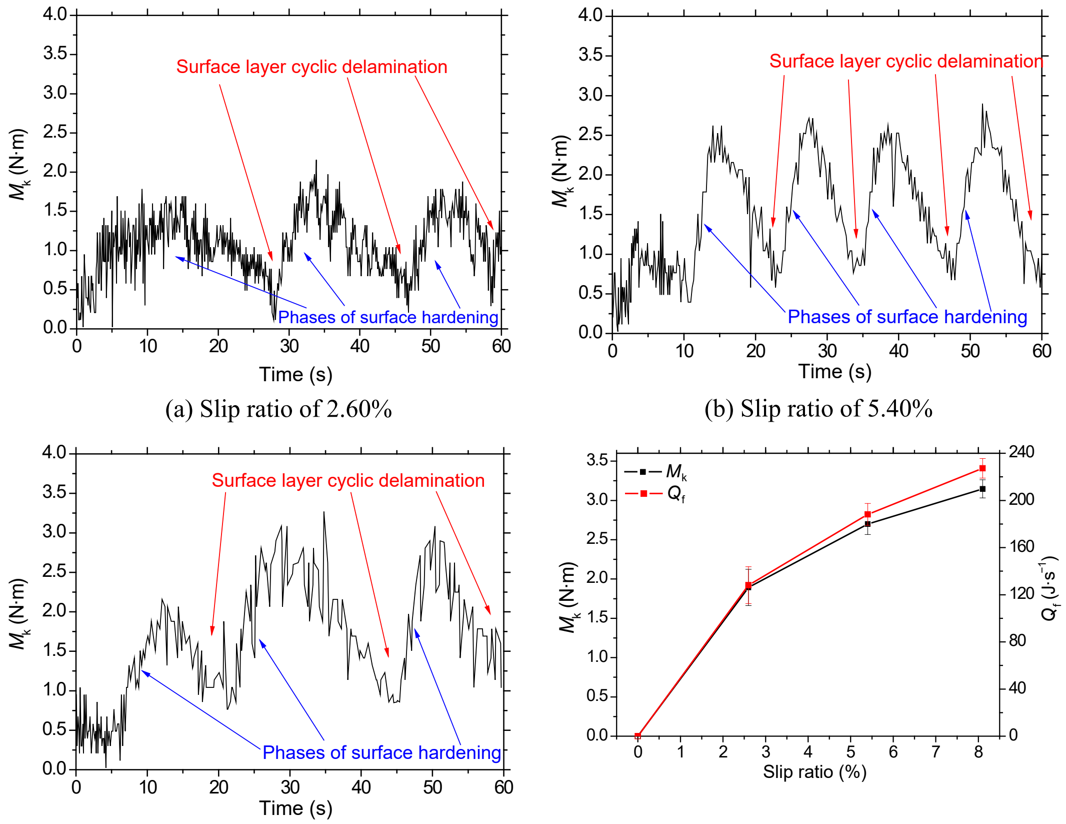

(a) Slip ratio of 2.60% (b) Slip ratio of 5.40%

(c) Slip ratio of 8.10 % (d) Evolution of M_k and Q_f along slip ratio

Fig. 5 (a–c) Records of M_k and (d) evolution of M_k as well as Q_f along the slip ratio.

drops down due to delamination of the heavily deformed near-surface region followed by the consequent strengthening phase (Fig. 5). This way, the cyclic behavior of M_k can be reasonably elucidated, as demonstrated later. Figure 5 also illustrates that the maximum of M_k and the corresponding F_f are higher for the higher slip ratios. Implementing the slip ratio makes the plastic deformation regime more complex, and the stress state in the sample/roller interface becomes more complicated. This, in turn, activates additional shear systems for dislocation slip within the fcc lattice. Consequently, surface strengthening increases at higher slip ratios, leading to higher maximum values of the measured M_k.

Considering Eqs. (2) and (3), the shear component F_f and the heat Q_f (related to the presence of the slip ratio) can be easily calculated. Figure 5(d) depicts a steep increase of the M_k (representing the maximums obtained from the M_k records depicted in Figs. 5(a)–5(c)) and Q_f as a function of the slip ratio. It is evident that the growth rate of Q_f is slightly more substantial than that of M_k due to the contribution of the accelerated v_{c2} (Table 3).

Figure 6 illustrates the three-dimensional (3D) views of the worn tracks where the rolling track (produced groove on the sample surface) is neighboring with the well-distinguishable extruded region. The simulations of the stress state reported in the previous work [16] (and also reported later in this study) clearly prove that the AISI 304 matrix is heavily yielded under the applied load, and very high stresses are localized in the narrow region of the sample/roller contact. Whilst the extruded region represents only the process of the plastic flow during which the yielded matrix in the sample/roller contact is transferred towards the side and becomes preserved on the sample surface, the developed worn track is a product of the synergistic contribution of two mechanisms. The first mechanism is related to the aforementioned mass transfer into the extruded region, and the second is governed by the step-by-step cyclic delamination of the near-surface layers in the rolling track due to the erratic nature of the strengthened layer. Having nomenclature as that shown in Fig. 7 and the surface profiles in TD as those depicted in Fig. 6, the extruded as well as track regions can be quantified (Figs. 8 and 9). The height of the extruded region H_2 is nearly unaffected by the slip ratio, whereas the depth of the produced track H_1 increases. The widths W_1 (worn track width) and W_2 (extruded region width) exhibit initial gradual growth, followed by saturation at higher slip ratios. The implementation of the slip ratio increases the integral area S_2 in the extruded region. However, this parameter remains nearly unaffected by variations in the slip ratio compared to the area and corresponding mass released in the worn track region (S_1). The increasing S_1/S_2 ratio suggests that mass transfer from the wear track to the extruded region dominates under pure rolling conditions. As the slip ratio increases, surface delamination in the wear track region accelerates, allowing the roller to penetrate deeper into the sample.

Figures 6–8 depict that the extruded region occurs only on the left side of the worn track and is fully missing on the opposite side. Such behavior is caused by the utilization of only one roller. The extruded regions formed on both sides of the worn track when two rollers were used, as reported in the previous study [16]. Despite the precise alignment of the angular position of the roller against the sample, the actual angle subtly deviates from 90°. Moreover, a further deviation is related to the inevitable shift (rotation due to bending—reported later) of the shaft (Fig. 2) during the transmission of M_k from the asynchronous motor to the shaft via the grooved belt.

The slip ratio affects not only the primary profile of the wear track or/and the extruded region but also the surface roughness

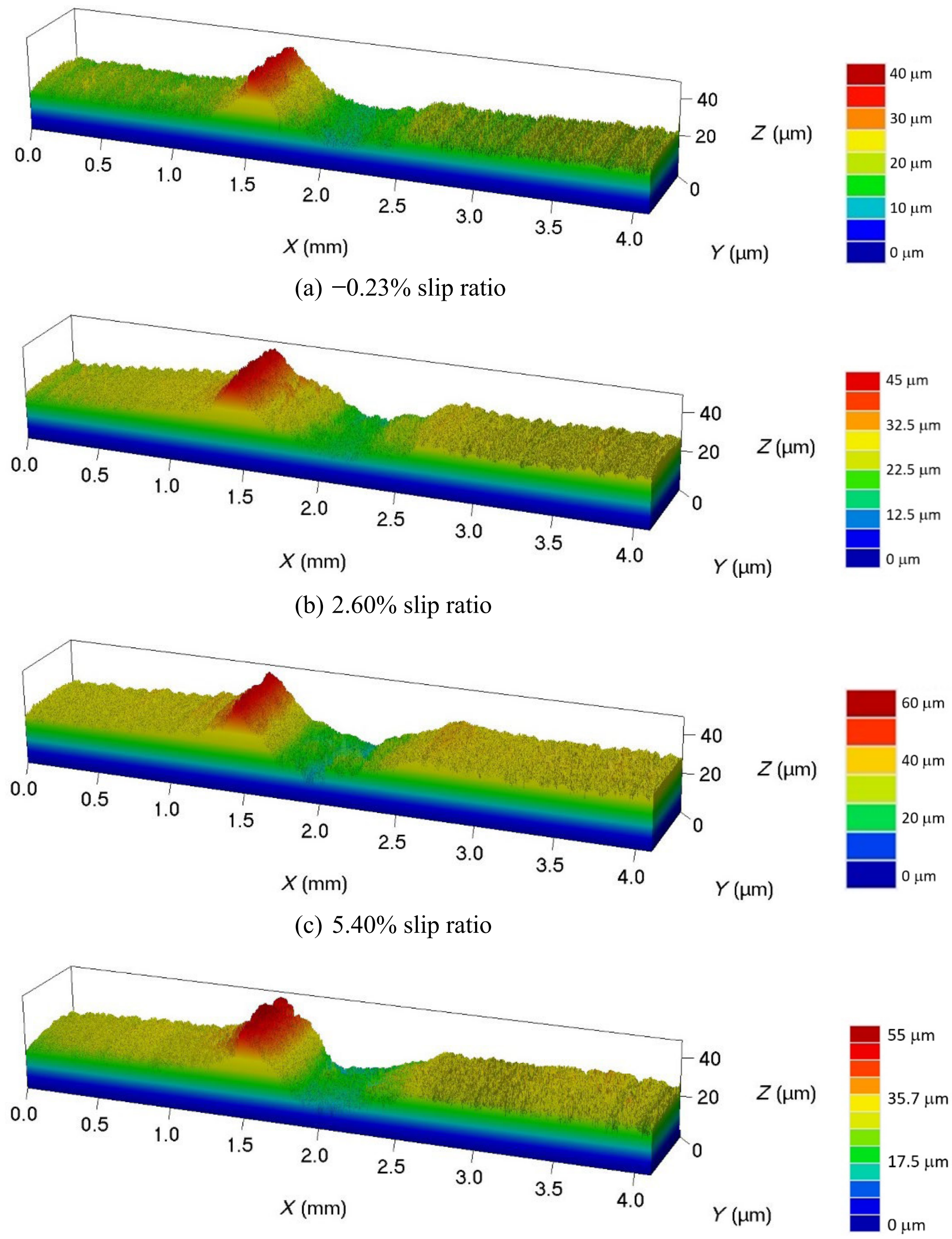

(a) −0.23% slip ratio

(b) 2.60% slip ratio

(c) 5.40% slip ratio

(d) 8.10% slip ratio

Fig. 6 3D views of the worn tracks as a function of slip ratio along TD.

(R_a). The height parameters expressed in term R_a exhibit slightly higher values for the surfaces generated with incorporated slip ratio, with the maximum slip ratio being 5.40%. However, it was found that the more complex mechanism of plastic work under the activated slip ratio also alters surface roughness skew (R_{sk}) and kurtosis (R_{ku}) parameters, significantly decreasing in RD. This indicates that the distribution function of surface roughness irregularities is also strongly affected (Table 6).

3.2 SEM and EBSD observations

Figure 10 illustrates SEM images of the grooves produced on the sample surface, composed of the wear track and extruded region, and their details for the different slip ratios. The deviation F_n in TD inevitably triggers the side flow of the austenitic matrix towards the extruded region and results in the heterogeneity of surface state with respect to the opposite sides of the wear track (Fig. 10(a)). The presence of the shear force F_s, forms the side plastic deformation flow along F_s in the direction towards the extruded region which is more substantial than in the opposite direction. The surface in the wear track becomes strained closely along F_s (the flow follows F_r (F_r is the resultant force obtained from the force vectors F_f and F_s) in Fig. 10(b)), and the initial delamination is initiated on the upper side of the track (on the side of the extruded region), whereas the opposite half is less affected. The same behavior with respect to the heterogeneity of surface state (opposite sides) can be reported for all samples (Fig. 10(c)).

Figures 10(c) and 10(d) also demonstrate that the delamination has already been initiated. Numerous microcracking and some delaminated spots can be observed complemented by the microgrooves in RD when the delaminated hard particles are dragged by the roller and grind the surface (Fig. 10(d)). The direction of the side flow is ineluctably altered due to presence not only F_s but also the superimposing contribution of F_f (Fig. 10(e)). Figure 10(e) also depicts that this side flow is disturbed in the delaminated regions and/or by the microgrooves.

A thorough inspection of Figs. 10(e) and 10(f) reveals that the direction of the side flow is altered, as F_s is approximately constant, while the F_f increases with the increasing slip ratio. This observation proves more complex plastic deformation at the higher slip ratios.

AISI 304 yielding can be verified by the calculation of the stress state and/or its simulation. Information about the developed stress within the contact area can be obtained from the Hertz model when the rolling contact regime is employed [46]. Due to the curved shape of the roller, the contact pressure p_m = 2.41 GPa can be obtained from the known F_n loading the contact region having the elliptical shape, where a is the half-axis along the RD direction and b along the TD as Eq. (5):

$$a = a^*\left(\frac{3F_nR'}{E'}\right)^{\frac{1}{3}},\ \ b = b^*\left(\frac{3F_nR'}{E'}\right)^{\frac{1}{3}} \tag{5}$$

where

$$a^* = \kappa\left[1+\frac{2(1-\kappa^2)}{\pi\kappa^2}-0.25\ln(\kappa)\right]^{\frac{1}{3}},\ \ b^* = \frac{a^*}{\kappa} \tag{6}$$

$$\frac{1}{\kappa} = 1+\left(\frac{\ln\left(\frac{16}{\lambda}\right)}{2\lambda}\right)^{\frac{1}{2}} - (\ln(4))^{\frac{1}{2}} + 0.16\ln(\lambda) \tag{7}$$

$$\lambda = \frac{R'_x}{R'_y}\ \text{or}\ \frac{R'_y}{R'_x} \tag{8}$$

where $a*$ and $b*$ are the non-dimensional semi-axes, E' is the

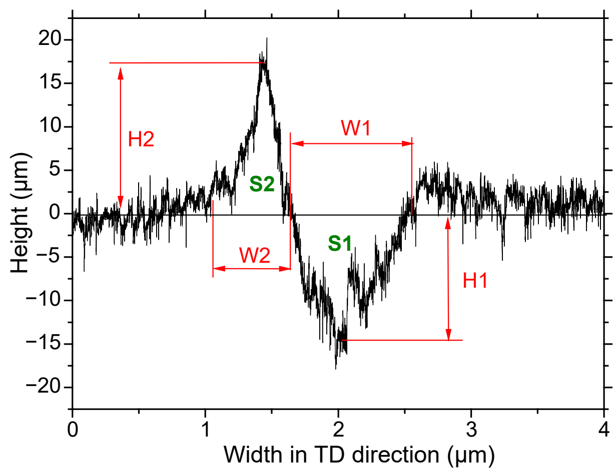

Fig. 7 2D profile of the worn track for slip ratio 5.40% with indicated nomenclature (red color).

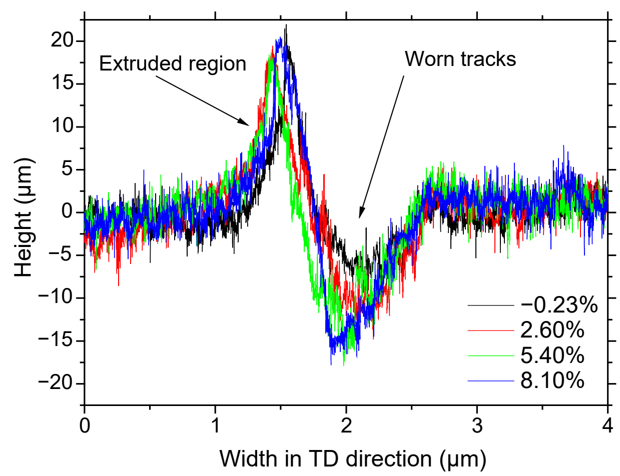

Fig. 8 Wear track profiles as a function of slip ratio.

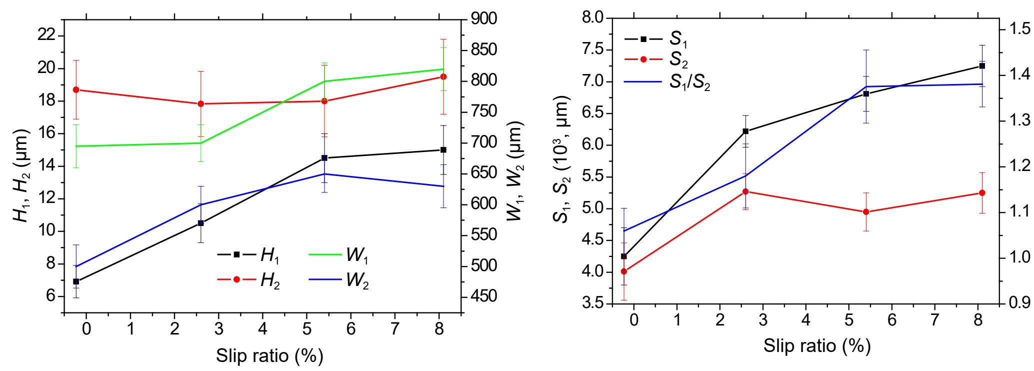

(a) Wear track heights and widths (b) Calculated S_1, S_2 as well as their ratios

Fig. 9 Wear track dimensions and the corresponding areas.

Table 6 Evolution of chosen surface roughness parameters as a function of the slip ratio

	RD				TD			
	−0.23%	2.60%	5.40%	8.10%	−0.23%	2.60%	5.40%	8.10%
R_a (m)	1.79±0.21	1.97±0.20	2.03±0.14	1.83±0.24	0.99±0.24	1.30±0.32	1.48±0.28	1.15±0.25
R_{sk} (—)	1.07±0.39	0.41±0.17	0.04±0.12	0.02±0.29	0.00±0.42	0.11±0.52	0.03±0.33	0.43±0.26
R_{ku} (—)	5.14±1.25	3.78±0.67	3.10±0.32	3.28±0.86	4.13±1.38	3.68±0.77	3.16±0.60	3.85±0.68

Note: Initial values of surface roughness before the rolling: in RD, R_a = 0.90±0.03 m, R_{sk} = 0.23±0.17, R_{ku} = 3.96±0.58; in TD: R_a = 0.84±0.10 m, R_{sk} = 0.10±0.32, R_{ku} = 3.71±0.36.

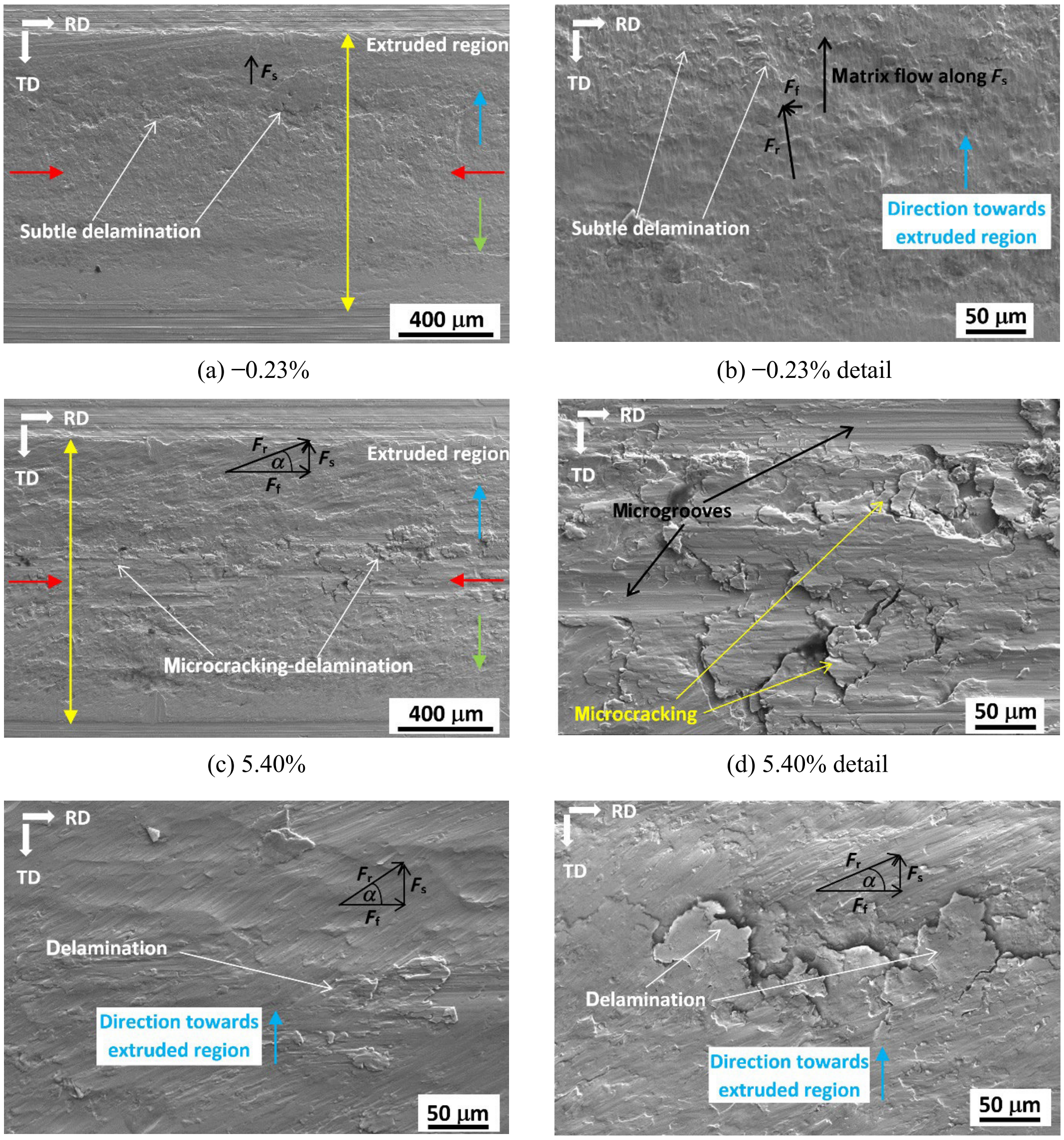

(a) −0.23% (b) −0.23% detail (c) 5.40% (d) 5.40% detail (e) 2.60% detail (f) 8.10% detail

Fig. 10 SEM images of the track surface after rolling. Yellow line: the wear track width; red arrows: the wear track center; blue arrow: the direction towards the extruded region; green arrow: the direction opposite with respect to the extruded region.

effective modulus of elasticity, R' is the effective radius, κ is the non-dimensional geometrical coefficient, λ is the ratio of the effective radii and atakes the smallest value of these quotients in Eq. (8), R'_x is the effective radius in the perpendicular direction against the rolling direction, and R'_y is the effective radius along the rolling direction. For further details, please follow the previous study [16].

Figure 11 demonstrates the distribution of the contact pressure along the wear track width (Fig. 11(a)) as well as along the rolling direction (Fig. 11(b)) based on the finite element method (FEM) simulation (details of simulations are indicated in Table 7). The obtained p_m for the FEM simulation is 2.12 GPa, which is close to the analytical approach and proves severe plastic deformation of the sample surface in the sample/roller contact. Figure 10 demonstrates the steep stress gradient along all directions when the direction of F_n is perpendicular to TD. As soon as the precession of F_n under the altered angle (Fig. 11) is considered, the stress distribution (as depicted in Fig. 11(a)) should rotate towards the extruded region with respect to TD. The symmetry of the wear track is disturbed; the degree of surface damage prevails in the wear track half linked with the blue arrow in Fig. 10 at the expense of the less affected opposite half linked with the green arrow. Figure 11 depicts that the maximum of the stresses can be found at a certain depth (indicated by the dotted line), resulting from the static solution. As soon as the motion of the roller and the sample is integrated (the dynamic solution), the stress profiles relocate as indicated by the black arrows, and the stress maximum is directly on the free surface [46]. Furthermore, this stress distribution also slightly shifts backward with respect to the rolling direction, as indicated in Fig. 11(b) [46].

The F_s component can be calculated when the angle is obtained from the SEM images (Fig. 10) knowing the F_f components ($F_s = F_f \times \mathrm{tg}\alpha$). This angle occurs in a certain range for each slip ratio as a result of variable contribution of F_f (F_f is not constant but follows the up and down evolution of M_k depicted in Fig. 5). Furthermore, F_s alters as a result of small sample runout and increases with the increase in the slip ratios due to growing α (stronger shaft bending). α drops down with the increasing slip ratio, but F_s is nearly unaffected since the increasing contribution of α is compensated by the growing F_f (Fig. 12). F_f for the slip ratio

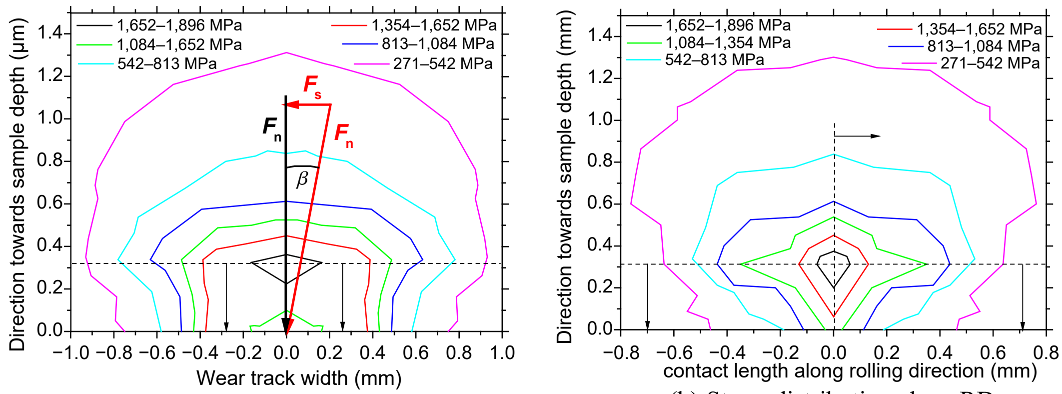

(a) Stress distribution along the track width (b) Stress distribution along RD

Fig. 11 Distribution of the contact stress along the track width as well as along RD (FEM simulation, static solution).

Table 7 FEM simulation details

Software: Ansys Workbench	Load: 1,002 N
E = 200 GPa Poisson's ratio = 0.29	Applied functions: fixed support and support displacement
Sample surface: target body, Hex dominant	Net: 348,177 nodes and 81,321 elements

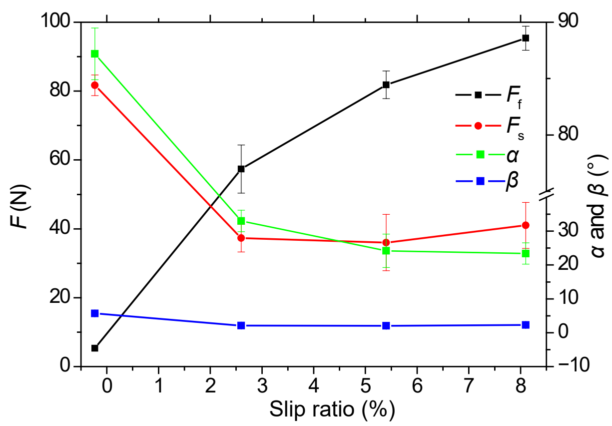

Fig. 12 Evolution of F_f, F_s, α, and β along with the slip ratio.

−0.23% can be obtained by the extrapolation of the M_k evolution in Fig. 5(d). Figure 10(b) depicts its opposite direction for the pure rolling as compared with the integrated slip ratios which results into the high α angle. β angle is about 2° for the slip ratios and about 5.7° for the pure rolling, which means that the F_n precession due to the static sample misalignment against the roller and sample run out prevail over the shaft bending as a result of the torque transmission.

Preferential straining of the matrix along RD (Fig. 13) under the slip ratio regime [35, 41] is governed particularly by the presence of F_f. SEM images depict the fiber-like microstructure in proximity to the surface and the micro-cracks, which will trigger the delamination in the further rolling contact cycles due to fully consumed plasticity in the heavily deformed surface under a multiaxial loading regime.

Inverse pole figures (IPFs) in Fig. 14 illustrate extreme grain fragmentation. Its degree and depth extent increase with the increasing slip ratio because of the dislocation saturation and formation of new grain boundaries inside the parental grains [47]. The dislocation density expressed in kernel average misorientation (KAM) is substantially growing (especially its depth extent) when comparing pure rolling and integrated slip ratio (Fig. 14). The near-surface layer is mostly composed of SIM with a limited fraction of parental austenite, which fraction is ascending towards the bulk. The depth in which the dominant fraction of the SIM occurs clearly grows with the slip ratio. The KAM and phase maps also demonstrate that the sandwich-like structure is developed primarily at the higher slip ratios. The heavily deformed sub-surface zone, which appears white in the KAM maps and the mixture of the red-green colors in the phase maps, is formed on the thermally softened region (see the region of vanishing dislocations underlying the white surface layer in the KAM maps). This thermally softened region appears predominantly green in the phase maps (Fig. 14). Finally, the deeper layers are a mixture of the SIM and the prevailing parental austenite. Some localized SIM islands can be found at a depth where (under the steeply decreasing stress from the surface) only those grains underwent

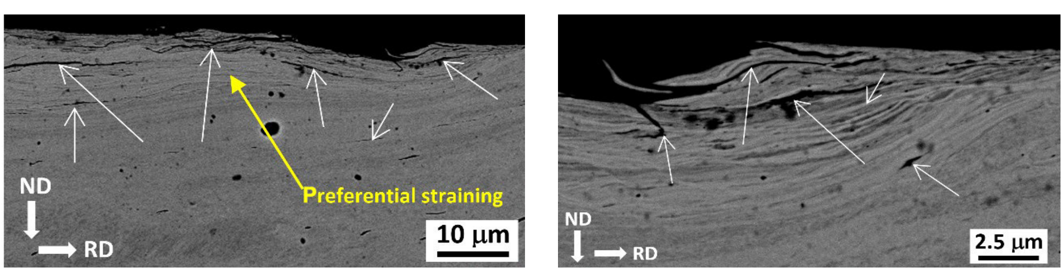

(a) Slip ratio 8.10% (b) Detail

Fig. 13 SEM images of the preferentially strained surface.

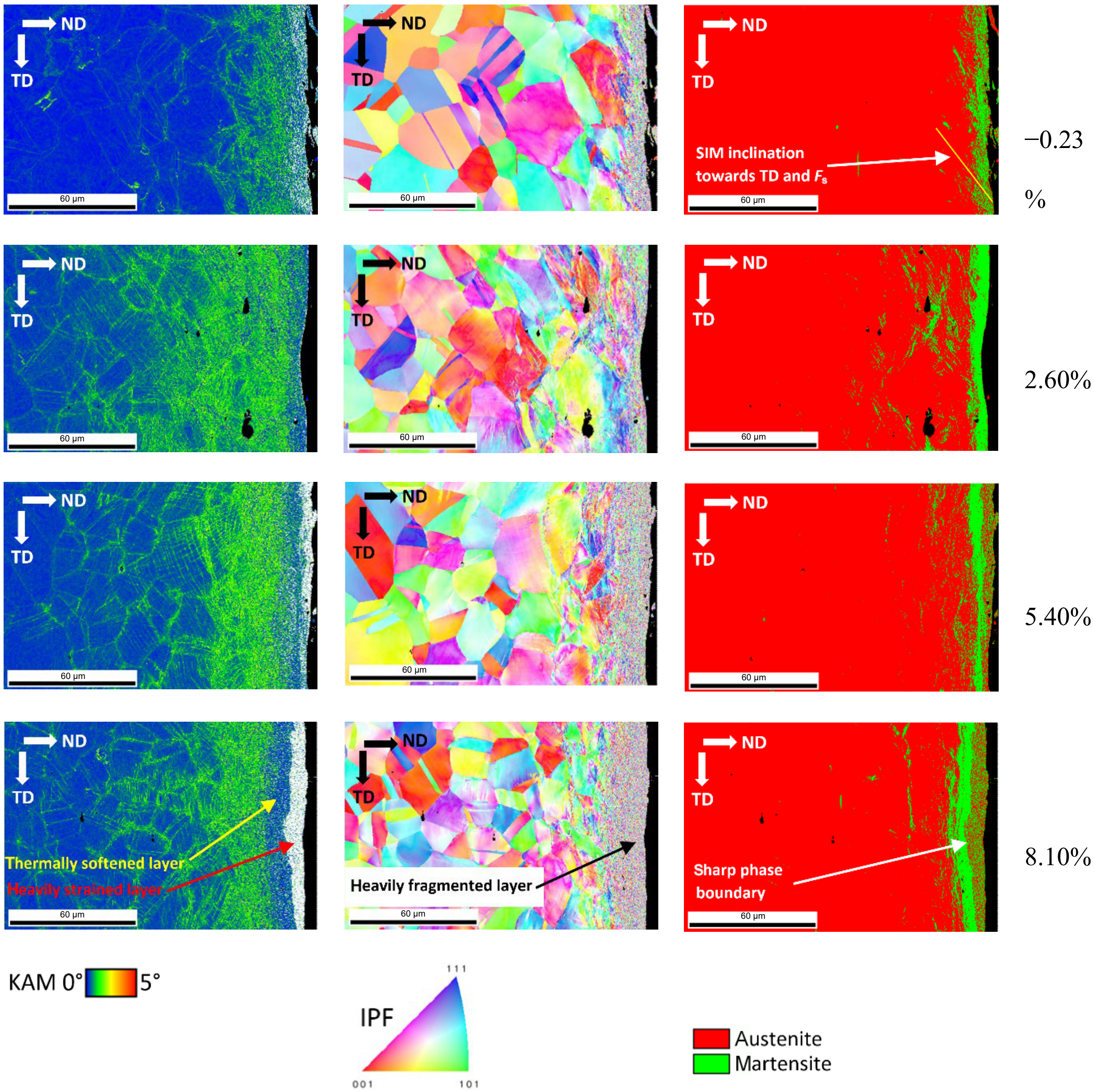

Fig. 14 EBSD images as a function of slip ratio.

the dislocation slip and/or phase transition because of the suitably oriented shearing direction with respect to the direction of the diminishing stress.

Figure 15(a) clearly proves information about the thermal softening within the region mainly composed of SIM. The HV0.025 within the softened region (the blue one in the KAM) is lower than that in the heavily strained one (the white one in the KAM). The further subsequent drop in HV0.025 is linked with the region mainly composed of austenite (remarkably softer phase as contrasted against SIM) being work hardened (green one in the KAM) followed by the less region in which HV0.025 falls down close to the bulk values. It is considered that the valuable and comparable SIM fraction can be found within the heavily strained as well as softened layers. However, the heavily strained region exhibits extremely fine-grained fragmentation and very high dislocation density, which raises some difficulties in EBSD indexing within this layer. For this reason, the green-red mixture can be obtained for the phase maps at the higher slip ratios (Fig. 14).

The presence of the sandwich-like microstructure is very important concerning surface delamination. Figures 14 and 15(b) demonstrate that the boundary between the first and second layers is quite sharp and mostly without a transitional region, indicating a rather sharp microstructure gradient. This boundary represents a weak zone, leading to the formation of microcracks that propagate along this sharp interface. After the delamination of the first heavily deformed layer, the plastic deformation propagates to the highly deformed (green in KAM maps) region, which already contains a high volume fraction of the SIM. Such a mechanism explains why M_k in Fig. 5 after the delamination phase at the higher slip ratios does not fall to the initial value, but the local minimum increases (Figs. 5(b) and 5(c))—due to the opposition of layers having the strain-hardened austenite and containing a high fraction of the SIM. On the other hand, the surface corresponding to the slip ratio of 2.60% has a less complicated structure—the heavily deformed layer is missing, and M_k maximums and minimums are lower.

As visualized in the KAM maps for all surfaces under the integrated slip ratios, the thermally softened region results from the conversion of energy transformed during rolling into heat, leading to a corresponding temperature increase. This aspect is

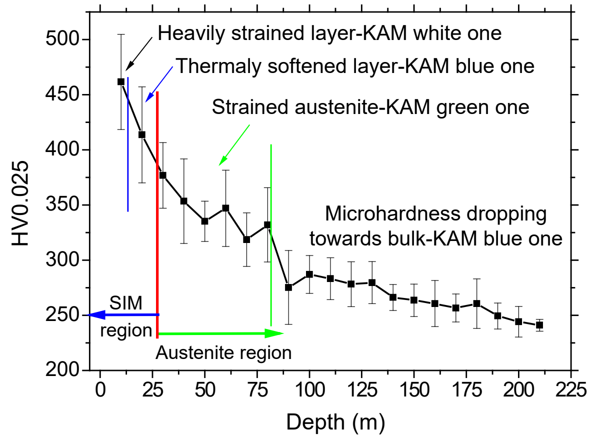

(a) Mirocrohardness depth profile for slip ratio 8.10%

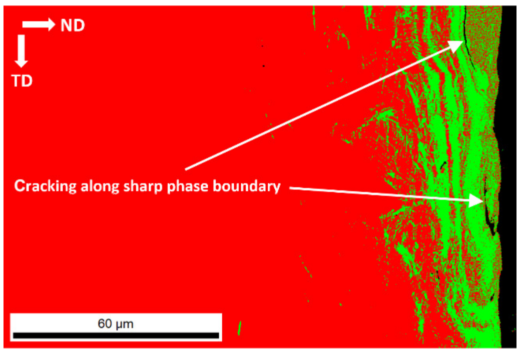

(b) Cracking along the phase boundaries

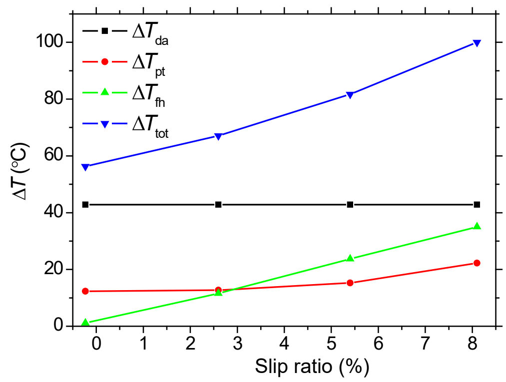

(c) Temperature as a function of the slip ratio

Fig. 15 (a) Microhardness depth profile for slip ratio 8.10%. (b) Phase map for slip ratio 8.10%, showing cracking along sharp phase boundaries. (c) Temperature increase as a function of slip ratio.

quite important and needs deeper insight. When the superimposing contribution of the thermal and contact stress is considered, the higher plastic deformation should be developed [39]. The temperature growth ΔT_{tot} in the sample/roller interface in this particular case is composed of 3 superimposing components (Fig. 15(c)):

$$\Delta T_{\text{tot}} = \Delta T_{\text{da}} + \Delta T_{\text{pt}} + \Delta T_{\text{fh}} \tag{9}$$

ΔT_{da} is the component associated with the plastic deformation of austenite with respect to its stress (σ)–strain (ε) curve and can be expressed as Eq. (10) [13]:

$$\Delta T_{\text{da}} = \frac{0.9}{C_p \rho} \int \sigma \mathrm{d}\varepsilon \tag{10}$$

When it is considered that 90% of plastic work is converted into heat, c_p is the thermal capacity (500 J·kg $^{-1}$·K^{-1}), and ρ is the density (7,950 kg·m^{-3}). This component can be calculated when the stress–strain curve of AISI 304 is measured during the uniaxial stress state (Fig. 15(c)). However, the true stress state under the pure rolling is far from the uniaxial one. Furthermore, this component should be enhanced for higher slip ratios since the higher number of slip systems is activated under a more complex stress state, as contrasted with the uniaxial tensile test and/or pure rolling [35, 42]. Therefore, this component would be higher than that depicted in Fig. 15(c), slightly growing along the slip ratios.

ΔT_{pt} is the component associated with the heat released during the phase transformation of austenite into the SIM and can be expressed as Eq. (11) [13]:

$$\Delta T_{\text{pt}} = \frac{H_{\text{m}} \cdot \Delta f_{\text{m}}}{C_p \cdot \rho} \tag{11}$$

where H_{m} is the enthalpy linked with the phase transformation of austenite into SIM (about 10,000 J·kg^{-1}), and Δf_{m} is the volume fraction of the strain-induced martensite. The fraction of the strain-induced martensite is gradually growing with the slip ratio and penetrates deeper. Therefore, the ΔT_{pt} should be higher, especially at the higher slip ratios. On the one hand, the increasing temperature favours the austenite phase at the expense of the strain-induced martensite. On the other hand, this effect is compensated by the prevailing effects of the plastic deformation, which becomes more severe at the higher slip ratios [35, 45] as well as the higher number of deformation cycles due to the higher v_{c2}. Elevated temperatures also enable the obtaining of a higher fraction of SIM at lower stresses [42].

Finally, ΔT_{fh} is the component linked with the friction heating expressed as Eq. (12) [48]:

$$\Delta T_{\text{fh}} = \frac{\mu \times F_{\text{f}} \times v_{c2}}{3 \times a \times \lambda_{\text{c}}} \tag{12}$$

where a is half of the contact length between the roller and the sample, and λ_{c} is the thermal conductivity of the AISI 304 (16.2 W·m^{-1}·K^{-1}) as contrasted against the thermal conductivity of the roller (41 W·m^{-1}·K^{-1}). 1/3 in Eq. (12) is due to the heat partitioning in the roller/sample interface as a result of their different λ. The ΔT_{fh} is increasing along the slip ratio due to the increasing sample speed v_{c2} as well as F_{f}, and it is gently hindered by the growing sample/roller contact area (linked with a, obtained from Fig. 11).

The data shown in Fig. 15(c) represents the average temperature increase within the elliptical sample/roller contact region. It is considered that due to the steep stress gradient (Fig. 11) the maximum temperature in the contact attains much higher values [39].

3.3 XRD measurements

The presence of the SIM in the parental austenite proves XRD diffraction patterns, as depicted in Fig. 16. Rolling wear produces compressive residual stresses of relatively high amplitude, especially at RD. Figure 17 shows that the amplitudes of compressive residual stresses, dislocation density in austenite, and SIM are mostly unaffected or slightly increased, comparing slip ratios of −0.23% and 2.60%. The reason is that the thermal softening in these cases is of a lower degree, and both surfaces exhibit very limited surface delamination, with only a few isolated spots. The severe drop in residual stresses at higher slip ratios is primarily driven by the onset of initial delamination, particularly at a slip ratio of 5.40%, along with the complementary effect of thermal softening. The specific contribution of thermal softening, however, cannot be easily isolated. Surface microcracking releases stress in the delaminated regions, while the activation of a higher number of shearing systems at the higher slip ratios, under the highly complex stress state [35, 45], leads to a rapid increase in dislocation density (especially in SIM, Fig. 17(b)). The degree of the surface microcracking (delamination) also explains the highest R_a for slip ratio 5.40% in RD and TD, see Table 5.

The peculiar evolution of the SIM weight fraction (Table 8) is ascribed to the strong preferential orientation of the near-surface matrix, as depicted in Fig. 13. Even from the obtained diffraction records, it was evident that the intensity of individual diffraction lines deviated from the tabulated values. For such a significantly preferentially directed structure, the Rietveld method, which uses the intensities of the individual diffraction maxima to calculate the mass distribution, is burdened with a large error.

From the statistical point of view, the SIM weight fractions (indicated in Table 8 as a function of the slip ratio) are mostly similar within the calculated standard deviations. On the other hand, the SIM penetration depth systematically grows along the slip ratio (Fig. 14 and Table 8). Furthermore, one has to take into account that the effective penetration depth of the used radiation is about 10 m, but the SIM depth varies from about 8 to 21 m (Table 8).

The phase maps in Fig. 14 show that in the surface layer of

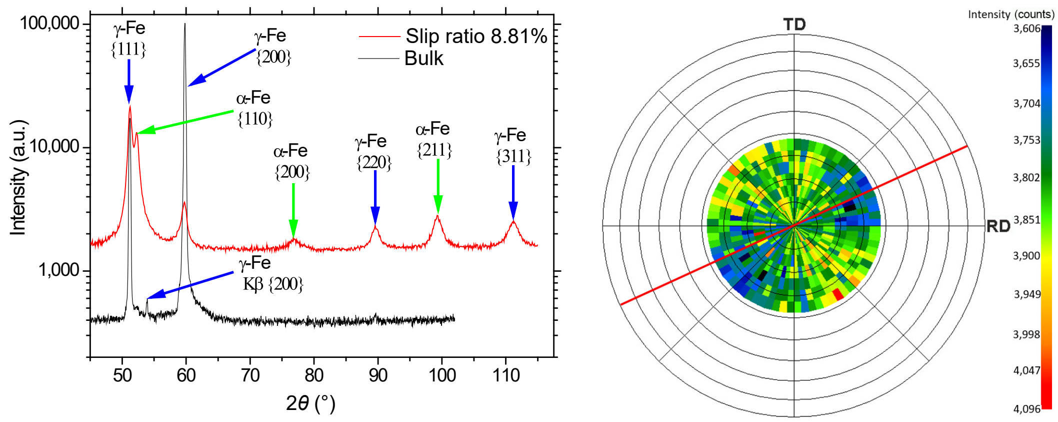

Fig. 16 (a) XRD diffraction patterns for the bulk and the slip ratio 8.10%, and (b) XRD pole figure of planes {311} of austenite for a slip ratio of 5.40%.

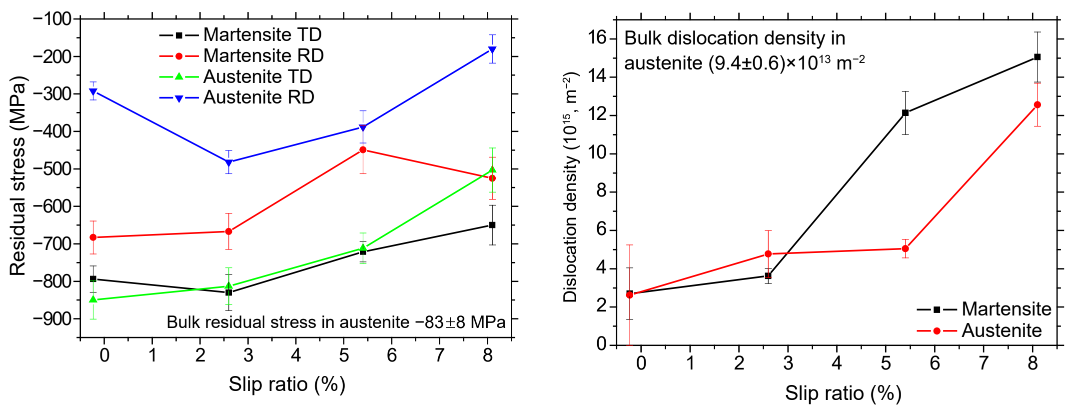

Fig. 17 Residual stresses and dislocation density as a function of slip ratio.

Table 8 Martensite weight fraction as a function of slip ratio

Slip ratio	−0.23%	2.60%	5.40%	8.10%
Martensite weight fraction (%)	55.2±11.7	47.1±8.4	41.9±1.1	52.4±7.6
Penetration depth of SIM (m)	8.5±2.1	8.75±1.9	10.5±1.7	17.3±3.1

Note: *The SIM penetration depths were obtained from the phase maps in Fig. 14 as the depth in which SIM dominates.

10 m, approximately half of the SIM is always present. A heavily deformed sub-surface layer is formed with a higher slip ratio, where austenite is slightly dominant. This explains the observed martensite weight fraction dependence measured by XRD.

Figure 16(b) shows only one {311} austenite pole figure for a slip ratio of 5.40%. The red line is inclined to the rolling direction by 25°. The diffracted intensity is symmetric along this line, indicating that the matrix is oriented at an angle corresponding to the rolling force relationships discussed earlier (Fig. 12 and the evolution of α in Fig. 10).

3.4 MBN measurements

The filtered MBN signals (Fig. 18) exhibit distinct MBN bursts when the magnetizing current and the corresponding magnetic field cross zero. The height of these bursts, as well as the corresponding MBN, grows in RD with the slip ratio (Figs. 19 and 20). The single peak burst in RD can be put in contrast against the MBN in TD (Fig. 18(d)), containing two well-distinguishable bursts. Moreover, the MBN signal in TD is higher for pure rolling compared to regimes with slip ratios. Additionally, MBN in TD is higher than in RD, leading to an increasing MBNRD/MBN^{TD} ratio (Figs. 19 and 20).

MBN is a function of the number of detected MBN pulses n and their magnitude X_i as Eq. (13):

$$\mathrm{MBN\ (RMS)} = \sqrt{\frac{1}{n}\sum_{i=1}^{n} X_i^2} \tag{13}$$

The strength of MBN pulses distinctly grows along the slip ratio, and the strength in RD is substantially higher than in TD.

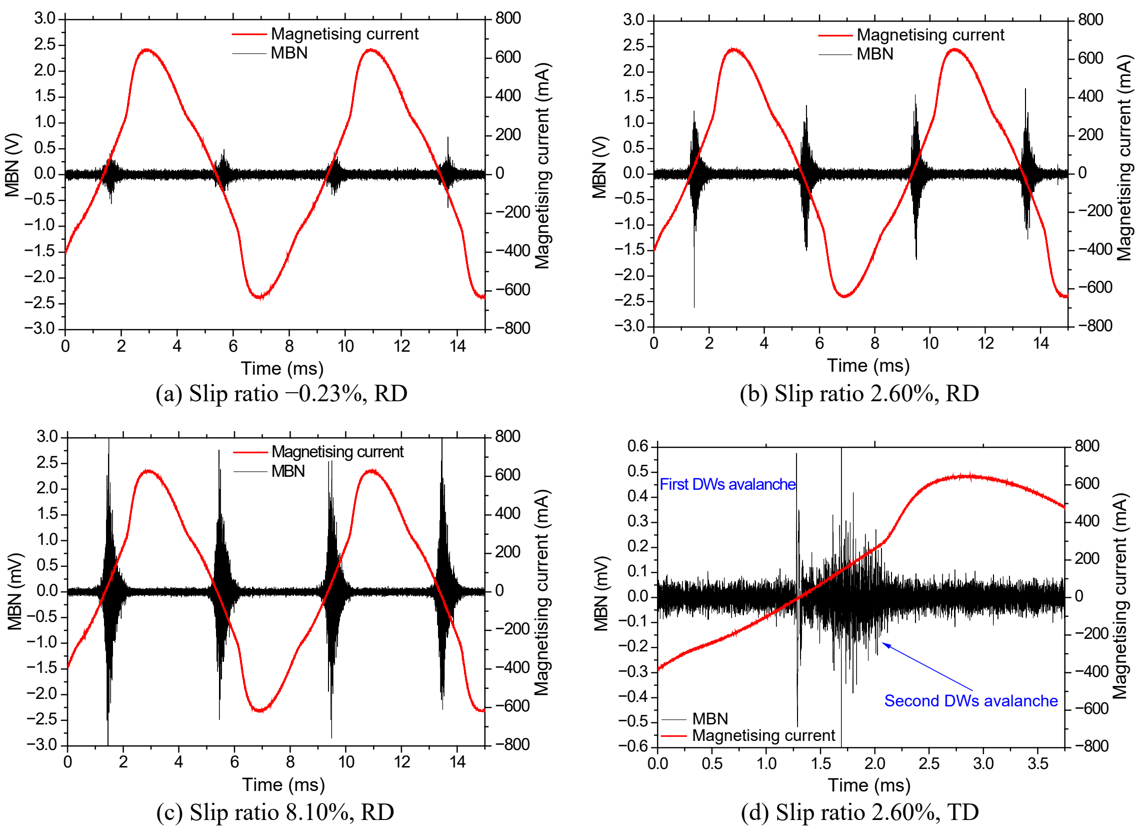

Fig. 18 MBN signals as a function of slip ratio and direction of measurement.

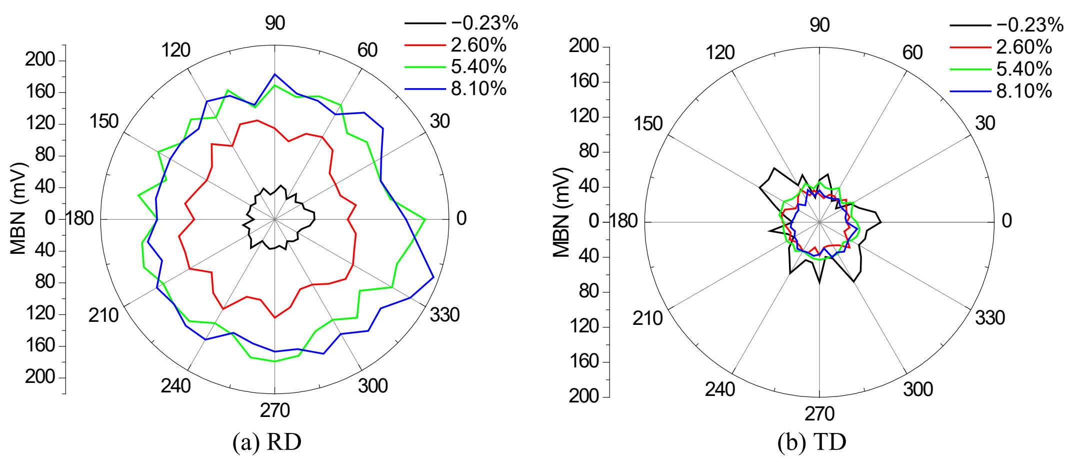

Fig. 19 Angular evolution of MBN in RD and TD as a function of the slip ratio.

Also, the number of detected MBN pulses is lower for pure rolling as compared to those associated with the slip ratios. With higher MBN in RD and lower MBN in TD for surfaces produced under integrated slip ratios, it can be concluded that the number of MBN pulses plays a complementary role in MBN analysis, with the strength of the recorded MBN pulses being the dominant factor.

Once the pulses within the background threshold are cut off, the number of MBN pulses decreases dramatically and follows a logical pattern (progressively increasing with slip ratio for RD and fewer MBN pulses in TD for slip ratio regimes) (Table 9). This post-processing of MBN data also offers a better opportunity to distinguish between MBN in RD for 5.40% and 8.10% slip ratios, where the saturation phase is more apparent in the conventional data processing (Fig. 20(b)).

The single peak MBN envelopes in RD (Fig. 21(a)) correspond to the single burst DWs avalanche in the detected MBN signals, and the two separated avalanches in TD are reflected by the two peak profiles of MBN envelopes in TD (Fig. 21(b)). The height of the envelopes in RD (also expressed by feature PH) grows with the slip ratio and follows the increasing MBN in RD. These envelopes are shifted towards weaker magnetizing fields, which should be linked with better mutual commutations among the SIM island embedded in the parental austenite matrix. The avalanche motion of DWs occurs due to their mutual clustering [49, 50] when the magnetic exchange interaction is spanned through the paramagnetic components of the matrix. Increasing density of the SIM island as well as the closing paramagnetic gaps among them improve the triggering DWs motion in the neighboring ferromagnetic island [50, 51], which in turn decreases magnetic hardness in RD along with the slip ratio expressed in term PP. DWs clustering causes the MBN pulses originating from individual DWs to overlap in time. For this reason, the number of DWs contributing to the MBN is at least 2–3 orders more than the number of detected MBN pulses [52].

Figures 18–20 depict a strong growth of MBN despite only a slight increase in the depth extent of the SIM (Fig. 14) within the estimated MBN sensing depth of about 75 m [53]. This controversy cannot be overlooked, and a deeper analysis is necessary to find a reasonable explanation. DWs in the matrix

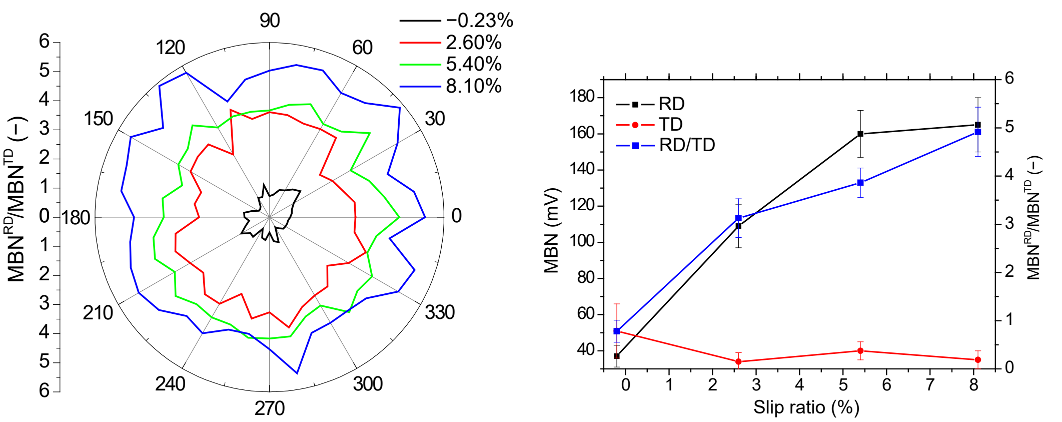

(a) angular evolution of MBN^{RD}/MBN^{TD} (b) MBN in RD and TD as well as MBN^{RD}/MBN^{TD}

Fig. 20 MBN and MBN^{RD}/MBN^{TD} as a function of slip ratio.

Table 9 Number of all detected and filtered (exceeding 75 mV) pulses

Direction	RD				TD			
Slip ratio	−0.23%	2.60%	5.40%	8.10%	−0.23%	2.60%	5.40%	8.10%
All pulses	18,642±680	25,717±492	25,012±323	25,170±492	17,174±421	25,446±328	26,952±994	26,343±642
Pulses over 75 (mV)	1,543±38	2,954±48	3,926±64	4,332±21	2,721 ±102	1,684±44	1,126±20	1,543±90
MBN over 75 (mV)	84±13	276±14	347±11	464±13	100±15	106±12	118±12	87±13

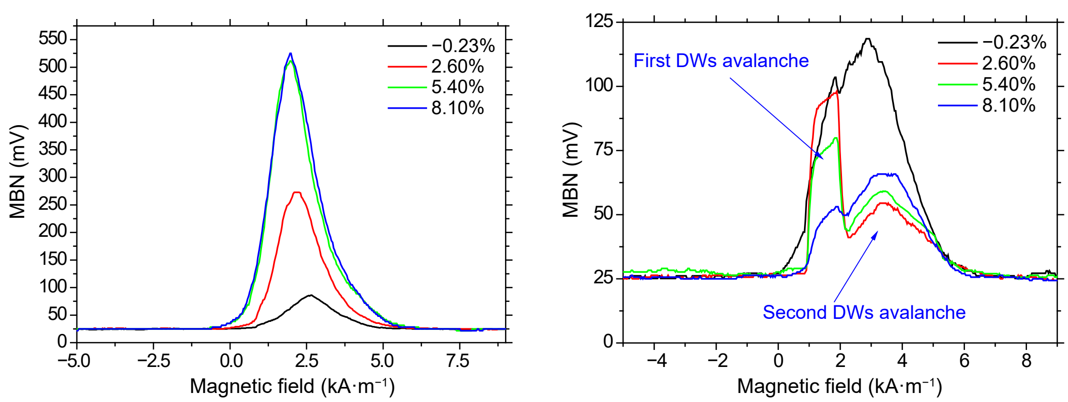

(a) RD (b) TD

Fig. 21 MBN envelopes in RD and TD as a function of slip ratio.

清华大学出版社 Tsinghua University Press | SciOpen

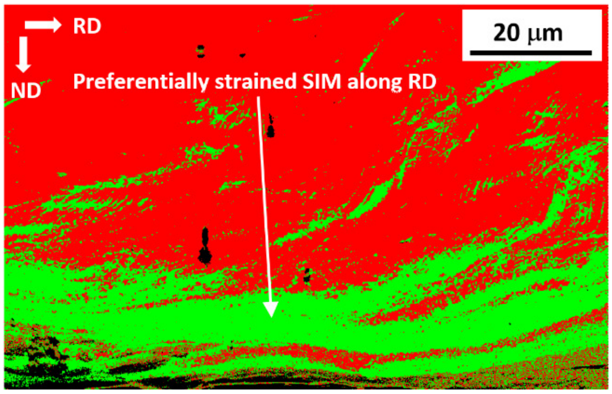

Fig. 22 Phase map for the slip ratio of 8.10% along RD.

composed of equiaxed grains are pinned by grain boundaries [32, 33]. As soon as a certain degree of preferential straining occurs, 180° DWs are crossing through the elongated grain boundaries [54]. SIM is preferentially aligned along the RD (Fig. 22). Therefore, DWs are also preferentially aligned in this particular case close to the direction of F_f at the higher slip ratios (F_f component dominates over F_s component) since DWs in the SIM are formed under the stress (DWs follow the direction of the resultant vector composed of F_f and F_s). Thus, randomly oriented DWs are replaced by preferentially aligned ones in RD at the expense of TD.

It is believed that the degree of this alignment increases with the rising F_f. This behavior leads to an increasing MBNRD/MBN^{TD} ratio and a reduction in the range of magnetic fields where DWs occur as the magnetic conditions for initiating irreversible DW motion become more similar due to their aligned direction. This, in turn, results in a lower full width at half maximum (FWHM) of the MBN envelopes (Fig. 23(a)). On the other hand, in the pure rolling regime, the F_f component is very low, and the F_s components dominate (Fig. 10(b)). Consequently, MBNRD/MBN^{TD} ratio is reversed (0.78).

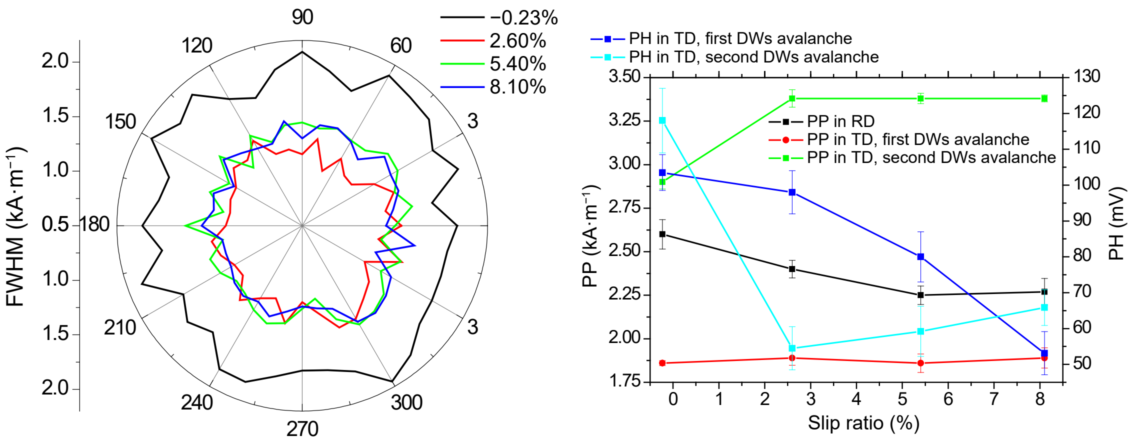

(a) FWHM (b) P and PH

Fig. 23 Evolution of (a) FWHM in RD and (b) PP as well as PH along with the slip ratio.

The situation associated with MBN in the TD is more complex. DWs motion occurs in the form of 2 avalanches, which in turn result in the double-peak profile of MBN envelopes (Fig. 21(b)). Peaks in TD for the pure rolling dominate due to alignment of DWs into TD as a result of low F_f and predomination of F_s. Once the slip ratio is integrated, the strong MBN emission during the first avalanche at the slip ratio of 2.60% is compensated by the weaker MBN emission during the second avalanche. The increasing slip ratio reverses this relationship due to the increasing F_f, which in turn results in nearly unaffected MBN in TD for the variable slip ratios (Figs. 20(b) and 23(b)).

Severe plastic deformation during rolling initiates surface oxidation [16]. The oxides are mostly the hard ferromagnetic phases attenuating MBN originating from the underlying non-corroded matrix [22, 30]. On the other hand, the thickness of the oxide film is very thin (mostly below 1 m) compared with the estimated MBN sensing depth (75 m). For this reason, the presence of these oxides on the surface only plays a minor role in MBN emission in this particular case.

4 Conclusions

The results of this study can be briefly summarised in the following points:

(1) The produced wear track exhibits strong asymmetry comprising extruded region only on one side due to the integration of only one roller.

(2) Material transfer into the extruded region prevails during pure rolling, whereas the surface delamination of the heavily deformed surface occurs at the higher slip ratios.

(3) The degree of the preferential straining in microstructure increases with the slip ratio due to the rising F_f component.

(4) The less affected subsurface follows near-surface heavily deformed region containing SIM. Surface delamination occurs mainly at the sharp boundary of these two layers.

(5) Thermal softening due to the increasing friction heating becomes apparent, especially at higher slip ratios. It manifests itself mainly by phase transformation and a more complicated stress state.

(6) The MBN increases along RD with the rising slip ratio due to the preferential straining of SIM in this direction, while the influence of residual stresses plays only a minor role.

This study demonstrates that Barkhausen noise emission can be effectively utilized to monitor austenitic steels susceptible to phase transformation into ferromagnetic martensite when subjected to rolling wear with an integrated slip ratio. However, it is essential to consider the cyclic behavior associated with repetitive cycles of surface strengthening followed by subsequent delamination. Longitudinal and/or transverse slip induces a complex stress state, which in turn reduces the phase stability of the austenitic matrix.

Acknowledgements

This work was financially funded by the EU NextGenerationEU through the Recovery and Resilience Plan for Slovakia under the Project No. 09I03-03-V04-00313.

Author contributions

Miroslav Neslušan: Conceptualization, Investigation, Supervision, Funding acquisition, Methodology, Project administration, Resources, Roles/Writing—original draft. Ronald Bašťovanský: Conceptualization, Investigation, Methodology. Peter Minárik: Data curation, Investigation, Software, Visualization, Roles/Writing—original draft. Karel Trojan: Data curation, Investigation, and software. Zuzana Florková: Data curation, Investigation, Validation, Visualization. Katarína Zgútová: Formal analysis, Investigation, Validation.

Availability of data and materials

The data that support the findings of this study are available from the corresponding author upon reasonable request.

Declaration of competing interest

The authors have no competing interests to declare that are relevant to the content of this article.

References

[1] Fonstein N. *Advanced High Strength Sheet Steels*. Cham (Switzerland): Springer, 2015.

[2] Berns H, Gavriljuk V, Riedner S. *High Interstitial Stainless Steels*. Berlin (Germany): Springer, 2012.

[3] Ma X, Tan W, Bonzom R, Mi X, Zhu G R. Impact-sliding fretting tribocorrosion behavior of 316L stainless steel in solution with different halide concentrations. *Friction* **11**(12): 2310–2328 (2023)

[4] Cui S G, Liu Y Z, Wang T, Tieu K, Wang L, Zeng D H, Li Z, Li W. Tribological behavior comparisons of high chromium stainless and mild steels against high-speed steel and ceramics at high temperatures. *Friction* **10**(3): 436–453 (2022)

[5] de Oliveira D A, Brito P P, de Castro Magalhães F, Azzi P C, Ardisson J D, Abrão A M. Influence of low plasticity burnishing on the formation of strain induced martensite in the surface layer. *J Mater Res Technol* **27**: 4573–4594 (2023)

[6] Gupta H, Kapoor R, Shinde D, Makineni S K. Achieving ultra-high flow stress and hardness in a medium Mn stainless steel by the formation of strain-induced martensite and G-phase precipitates. *Scripta Mater* **241**: 115892 (2024)

[7] Chen, H, Zhao, D, Wang, Q, Qiang Y, Qi J. Effects of impact energy on the wear resistance and work hardening mechanism of medium manganese austenitic steel. *Friction* **5**: 447–454 (2017)

[8] Aristeidakis J S, Haidemenopoulos G N. Constitutive and transformation kinetics modeling of ε-, α′-martensite and mechanical twinning in steels containing austenite. *Acta Mater* **228**: 117757 (2022)

[9] Olson G B, Cohen M. Kinetics of strain-induced martensitic nucleation. *Metall Trans A* **6**(4): 791–795 (1975)

[10] Brooks J W, Loretto M H, Smallman R E. *In situ* observations of the formation of martensite in stainless steel. *Acta Metall Mater* **27**(12): 1829–1838 (1979)

[11] Neyra Astudillo M R, Núñez N M, López Pumarega M I, Ferrari G, Ruzzante J, Gómez M. Study of martensite induced by deformation with Magnetic Barkhausen Noise technique. *J Magn Magn Mater* **556**: 169454 (2022)

[12] Haušild P, Kolařík K, Karlík M. Characterization of strain-induced martensitic transformation in A301 stainless steel by Barkhausen noise measurement. *Mater Design* **44**: 548–554 (2013)

[13] Haušild P, Davydov V, Drahokoupil J, Landa M, Pilvin P. Characterization of strain-induced martensitic transformation in a metastable austenitic stainless steel. *Mater Design* **31**(4): 1821–1827 (2010)

[14] Kleber X, Barroso S P. Investigation of shot-peened austenitic stainless steel 304L by means of magnetic Barkhausen noise. *Mater Sci Eng A* **527**(21–22): 6046–6052 (2010)

[15] Unal O, Varol R. Surface severe plastic deformation of AISI 304 via conventional shot peening, severe shot peening and repeening. *Appl Surf Sci* **351**: 289–295 (2015).

[16] Neslušan M, Bašťovanský R, Čep R, Minárik P, Trojan K, Florková Z. Phase transition in AISI 304 during rolling contact wear and its monitoring *via* Barkhausen noise emission. *Wear* **558**: 205563 (2024).

[17] Qu S, Huang C X, Gao Y L, Yang G, Wu S D, Zang Q S, Zhang Z F. Tensile and compressive properties of AISI 304L stainless steel subjected to equal channel angular pressing. *Mater Sci Eng A* **475**(1–2): 207–216 (2008)

[18] Mine Y, Horita Z, Murakami Y. Effect of hydrogen on martensite formation in austenitic stainless steels in high-pressure torsion. *Acta Mater* **57**(10): 2993–3002 (2009)

[19] Scheriau S, Zhang Z, Kleber S, Pippan R. Deformation mechanisms of a modified 316L austenitic steel subjected to high pressure torsion. *Mater Sci Eng A* **528**(6): 2776–2786 (2011)

[20] Nakao Y, Miura H. Nano-grain evolution in austenitic stainless steel during multi-directional forging. *Mater Sci Eng A* **528**(3): 1310–1317 (2011)

[21] Tikhonova M, Belyakov A, Kaibyshev R. Strain-induced grain evolution in an austenitic stainless steel under warm multiple forging. *Mater Sci Eng A* **564**: 413–422 (2013)

[22] Jiles D. *Introduction to Magnetism and Magnetic Materials*. Boca Raton (USA): CRC Press, 2015.

[23] Chikazumi S. *Physics of Ferromagnetism*, 2nd edn. UK: Oxford University Press, 2005.

[24] Bayramoglu S, Gür C H, Alexandrov I V, Abramova M M. Characterization of ultra-fine grained steel samples produced by high pressure torsion via magnetic Barkhausen noise analysis. *Mater Sci Eng A* **527**(4–5): 927–933 (2010)

[25] Neslušan M, Čížek J, Kolařík K, Minárik P, Čilliková M, Melikhová O. Monitoring of grinding burn via Barkhausen noise emission in case-hardened steel in large-bearing production. *J Mater Process Tech* **240**: 104–117 (2017)

[26] Anglada-Rivera J, Padovese L R, Capó-Sánchez J. Magnetic Barkhausen noise and hysteresis loop in commercial carbon steel: Influence of applied tensile stress and grain size. *J Magn Magn Mater* **231**(2–3): 299–306 (2001)

[27] Ktena A, Hristoforou E, Gerhardt G J L, Missell F P, Landgraf F J G, Rodrigues D L, Alberteris-Campos M. Barkhausen noise as a microstructure characterization tool. *Physica B* **435**: 109–112 (2014)

[28] Santa-aho S, Honkanen M, Kaappa S, Azzari L, Saren A, Ullakko K, Laurson L, Vippola M. Multi-instrumental approach to domain walls and their movement in ferromagnetic steels–Origin of Barkhausen noise studied by microscopy techniques. *Mat Des* **234**: 112308 (2023)

[29] Batista L, Rabe U, Altpeter I, Hirsekorn S, Dobmann G. On the mechanism of nondestructive evaluation of cementite content in steels using a combination of magnetic Barkhausen noise and magnetic force microscopy techniques. *J Magn Magn Mater* **354**: 248–256 (2014)

[30] Neslušan M, Bahleda F, Minárik P, Zgútová K, Jambor M. Non-destructive monitoring of corrosion extent in steel rope wires via Barkhausen noise emission. *J Magn Magn Mater* **484**: 179–187 (2019)

[31] Fagan P, Ducharne B, Daniel L, Skarlatos A, Domenjoud M, Reboud C. Effect of stress on the magnetic Barkhausen noise energy cycles: A route for stress evaluation in ferromagnetic materials. *Mater Sci Eng B* **278**: 115650 (2022)

[32] Liu J, Tian G Y, Gao B, Zeng K, Zheng Y, Chen J Z. Micro-macro characteristics between domain wall motion and magnetic Barkhausen noise under tensile stress. *J Magn Magn Mater* **493**: 165719 (2020)

[33] Qiu F S, Jovičević-Klug M, Tian G Y, Wu G H, McCord J.

Correlation of magnetic field and stress-induced magnetic domain reorientation with Barkhausen Noise. *J Magn Magn Mater* **523**: 167588 (2021)

[34] Neslušan M, Minárik P, Čep R, Uríček J, Trojan K, Ganev N, Trško L. Barkhausen noise emission of AISI 304 stainless steel originating from strain induced martensite by shot peening. *J Mater Res Technol* **20**: 748–762 (2022)

[35] Tosangthum N, Krataitong R, Wila P, Koiprasert H, Buncham K, Kansuwan P, Manonukul A, Sheppard P. Dry rolling-sliding wear behavior of ER9 wheel and R260 rail couple under different operating conditions. *Wear* **518**: 204636 (2023)

[36] Yang Y F, Ling L, Wang J C, Zhai W M. A numerical study on tread wear and fatigue damage of railway wheels subjected to anti-slip control. *Friction* **11**(8): 1470–1492 (2023)

[37] Argatov I I, Chai Y S. A theoretical justification of the slip index concept in fretting analysis. *Friction* **11**(7): 1265–1275 (2023)

[38] Wang D Z, de Boer G, Neville A, Ghanbarzadeh A. A numerical model to simulate the transient frictional viscoelastic sliding contact. *Friction* **12**(2): 319–339 (2024)

[39] Lian Q L, Deng G Y, Tieu A K, Li H J, Liu Z M, Wang X, Zhu H T. Thermo-mechanical coupled finite element analysis of rolling contact fatigue and wear properties of a rail steel under different slip ratios. *Tribol Int* **141**: 105943 (2020)

[40] Gao F M, Zhang L B, Zhou J, Xiong Y, Wu J, Fan J C. Evolution of tribo-magnetization during sliding of ferromagnetic materials. *Friction* **12**(5): 906–918 (2024)

[41] Zhao Y, Wong P L. Thermal-EHL analysis of slip/no-slip contact at high slide-to-roll ratio. *Tribol Int* **153**: 106617 (2021)

[42] Sohrabi M J, Naghizadeh M, Mirzadeh H. Deformation-induced martensite in austenitic stainless steels: A review. *Arch Civ Mech Eng* **20**(4): 124 (2020)

[43] Noh H S, Kang J H, Kim K M, Kim S J. Different effects of Ni and Mn on thermodynamic and mechanical stabilities in Cr–Ni–Mn austenitic steels. *Metall Mater Trans A* **50**(2): 616–624 (2019)

[44] Santos L L, Cardoso R P, Brunatto S F. Direct correlation between martensitic transformation and incubation-acceleration transition in solution-treated AISI 304 austenitic stainless steel cavitation. *Wear* **462**: 203522 (2020)

[45] Blažek D, Neslušan M, Mičica M, Pištora J. Extraction of Barkhausen noise from the measured raw signal in high-frequency regimes. *Measurement* **94**: 456–463 (2016)

[46] Beek A. *Advanced Engineering and Reliability*. The Netherlands: TU Delf, 2006.

[47] Tang Y H, Ji P F, Li B, Zhang G F, Ma W, Wang F, Zhang X Y, Ma M Z, Liu R P. Effect of loading on microstructure and friction and wear behavior of an austenite lightweight steel. *Tribol Int* **177**: 108006 (2023)

[48] Hutchings I, Shipway P. Friction. In: *Tribology*, 2nd edn. UK: Butterworth-Heinemann, 2017: 37–77.

[49] Alessandro B, Beatrice C, Bertotti G, Montorsi A. Domain-wall dynamics and Barkhausen effect in metallic ferromagnetic materials. II. Experiments. *J Appl Phys* **68**(6): 2908–2915 (1990).

[50] Tadić B, Mijatović S, Janićević S, Spasojević D, Rodgers G J. The critical Barkhausen avalanches in thin random-field ferromagnets with an open boundary. *Sci Rep* **9**(1): 6340 (2019)

[51] Bertotti G, Fiorillo F. Bloch wall motion in Si–Fe investigated through surface emf measurements. *J Magn Magn Mater* **41**(1–3): 303–305 (1984)

[52] Neslušan M, Pitoňák M, Minárik P, Tkáč M, Kollár P, Životský O. Influence of domain walls thickness, density and alignment on Barkhausen noise emission in low alloyed steels. *Sci Rep* **13**: 5687 (2023)

[53] Stupakov A, Perevertov A, Neslušan M. Reading depth of the magnetic Barkhausen noise. II. Two-phase surface-treated steels. *J Magn Magn Mater* **513**: 167239 (2020)

[54] Hajko V, Potocký L, Zentko A. *Magnetization Processes*. Slovakia: Alfa Bratislava, 1982.

Miroslav Neslušan is a full professor at the University of Žilina in Slovakia, educated in the field of materials processing science and technologies, such as machining, forming, heat treatment, especially focused on metals. He investigates surface damage in terms of residual stresses, microstructure alterations, and the corresponding phase transitions. He is mainly focused on non-destructive monitoring of surfaces and bodies by the use of the electromagnetic Barkhausen noise technique.